



## Performance and cost of automotive fuel cell systems with ultra-low platinum loadings

R.K. Ahluwalia<sup>a,\*</sup>, X. Wang<sup>a</sup>, J. Kwon<sup>a</sup>, A. Rousseau<sup>a</sup>, J. Kalinoski<sup>b</sup>, B. James<sup>b</sup>, J. Marcinkoski<sup>c</sup>

<sup>a</sup> Argonne National Laboratory, Argonne, IL, United States

<sup>b</sup> Directed Technologies Inc., Arlington, VA, United States

<sup>c</sup> United States Department of Energy, Washington, DC, United States

### ARTICLE INFO

#### Article history:

Received 11 December 2010

Received in revised form 14 January 2011

Accepted 19 January 2011

Available online 26 January 2011

#### Keywords:

Polymer electrolyte fuel cells

Automotive fuel cell stacks

Electrocatalysts

Air management

Heat rejection

Cost and performance

### ABSTRACT

An automotive polymer-electrolyte fuel cell (PEFC) system with ultra-low platinum loading (0.15 mg-Pt cm<sup>-2</sup>) has been analyzed to determine the relationship between its design-point efficiency and the system efficiency at part loads, efficiency over drive cycles, stack and system costs, and heat rejection. The membrane electrode assemblies in the reference PEFC stack use nanostructured, thin-film ternary catalysts supported on organic whiskers and a modified perfluorosulfonic acid membrane. The analyses show that the stack Pt content can be reduced by 50% and the projected high-volume manufacturing cost by >45% for the stack and by 25% for the system, if the design-point system efficiency is lowered from 50% to 40%. The resulting penalties in performance are a <1% reduction in the system peak efficiency; a 2–4% decrease in the system efficiency on the urban, highway, and LA92 drive cycles; and a 6.3% decrease in the fuel economy of the modeled hybrid fuel-cell vehicle on the combined cycle used by EPA for emission and fuel economy certification. The stack heat load, however, increases by 50% at full power (80 kW<sub>e</sub>) but by only 23% at the continuous power (61.5 kW<sub>e</sub>) needed to propel the vehicle on a 6.5% grade at 55 mph. The reduced platinum and system cost advantages of further lowering the design-point efficiency from 40% to 35% are marginal. The analyses indicate that thermal management in the lower efficiency systems is very challenging and that the radiator becomes bulky if the stack temperature cannot be allowed to increase to 90–95 °C under driving conditions where heat rejection is difficult.

© 2011 Elsevier B.V. All rights reserved.

### 1. Introduction

Although polymer electrolyte fuel cells (PEFC) offer many advantages (higher efficiency, lower emissions, greater fuel flexibility, etc.) over internal combustion engines (ICE) for vehicle propulsion, they must also compete on the bases of cost and durability [1]. Fuel cell stack components need to demonstrate adequate durability under rapidly varying loads and idling conditions, and withstand thousands of startups and shutdowns that are typical of automotive duty cycles. A fuel cell system (FCS) needs to cost less than \$30–45 kW<sup>-1</sup> for the technology to be competitive with automotive ICEs that cost \$25–35 kW<sup>-1</sup>. Cost of platinum in electrocatalysts is a significant component of the overall cost of the PEFC stacks. Whereas researchers are trying to develop new catalysts and electrode structures to reduce the Pt loading (mg-Pt cm<sup>-2</sup>) [2,3], the focus of this paper is on assessing the impact of lowering stack and

system costs by reducing the amount of Pt used (i.e., g-Pt kW<sub>e</sub><sup>-1</sup>), while keeping fixed the Pt loading, on the fuel cell system efficiency and other performance parameters.

The main purpose of this study is to explore the relationship between the cost and performance of automotive fuel cell (FC) systems. We first present results of a systematic study to quantify the effect of varying the FCS efficiency at rated power,  $\eta_S(100\%)$  on the stack Pt content needed to achieve that value of  $\eta_S(100\%)$ . Next, we employ a high-volume manufacturing cost model to determine the costs of these PEFC stacks and FC systems and to define the relationship between  $\eta_S(100\%)$  and stack and system costs. Since light-duty vehicles on average spend considerable time at low loads, we also investigate the relationship between  $\eta_S(100\%)$  and the part-load performance (including the peak efficiency) of the FC systems. Finally, we conduct drive cycle simulations to determine the sensitivity of the vehicle fuel economy to varying  $\eta_S(100\%)$ . Taken together, the results can be used to assess the incremental penalty in fuel economy against the savings in system cost that can be realized by designing and manufacturing automotive FC systems with  $\eta_S(100\%)$  lower than 50%.

Heat rejection in automotive fuel cell systems is difficult because the PEFC stack operates at relatively low temperatures (<80 °C)

\* Corresponding author at: Argonne National Laboratory, Nuclear Engineering Division, 9700 S Cass Avenue, Argonne, IL 60439, United States.

Tel.: +1 630 252 5979; fax: +1 630 252 5287.

E-mail address: [walia@anl.gov](mailto:walia@anl.gov) (R.K. Ahluwalia).

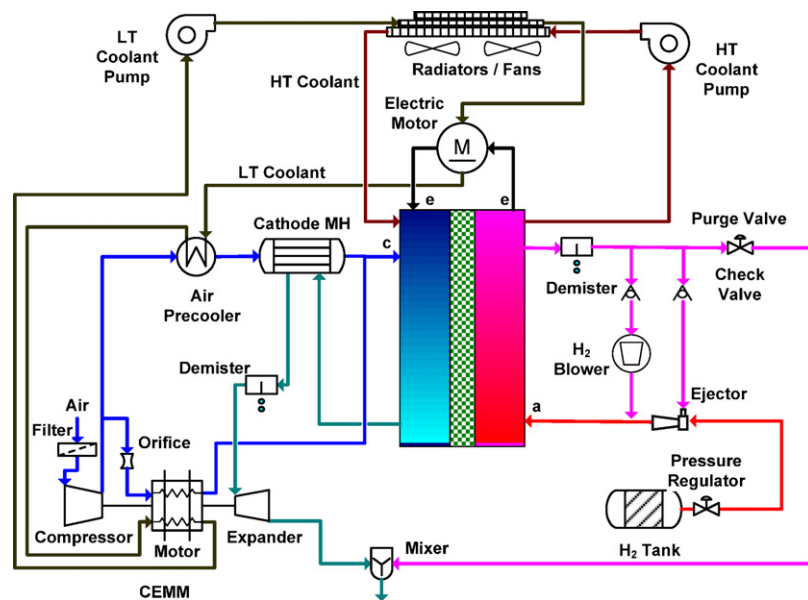


Fig. 1. Reference fuel cell system configuration.

[1,4]. It becomes even more challenging in FC systems with lower efficiencies and, consequently, higher heat rejection loads. In this paper, we analyze the conditions under which lower efficiency (and lower cost) systems may become unacceptable from the standpoint of heat rejection. The particular conditions analyzed are the average cell voltage corresponding to the design point of the heat rejection system, the maximum temperature to which the stack can be raised, and the ability of the air management system to allow operation at higher than normal operating pressures.

The air management subsystem has been identified as the second largest contributor (after the PEFC stack) to the overall cost of the FCS [5]. The studies also indicate that the motor and the motor controller are the two most expensive components of the air management subsystem. The estimated costs of the two components are proportional to their power rating, which is a function of the operating pressure and the air flow rate at the rated power condition. In this study, we assess the prospect of reducing the cost of the air management system by lowering the stack operating pressure at rated power. We also evaluate the impact of the design-point operating pressure on the design and performance of the heat rejection system.

## 2. Fuel cell system

Fig. 1 is a schematic of the 80-kW<sub>e</sub>-net reference FCS configuration that forms the basis of this study, additional details of which are given elsewhere [6]. The membrane electrode assemblies (MEA) in our study are assumed to be nanostructured, thin film, ternary PtCo<sub>x</sub>Mn<sub>y</sub> catalysts (NSTFC) supported on organic whiskers [2,3]. The NSTFC catalyst has shown significantly enhanced stability against surface area loss from Pt dissolution when compared to conventional Pt/C dispersed catalysts under both accelerated voltage cycling from 0.6 to 1.2 V and real-time start stop cycling [7]. Also, NSTFC support-whiskers have shown total resistance to corrosion when held at potentials up to 1.5 V for 8 h, conditions at which the conventional carbon support is severely corroded [7]. The NSTFC electrodes are hot-press laminated with a modified perfluorosulfonic acid (PFSA) membrane that has a reduced number of carboxylic end groups, compared to Nafion®, and an 850 equivalent weight that, with or without chemical stabilization and mechanical reinforcement, has shown good oxidative stability in

load cycling tests at 90 °C for >4000 h [7]. The cells use non-woven carbon gas diffusion layers (GDL) with microporous layers (MPL) and the flow fields are assumed to be stamped from thermally nitrated Fe–20Cr–4V alloy foils [8].

The air management subsystem consists of a compressor–expander module (CEM) with a liquid-cooled motor, mixed axial and radial flow compressor, variable-nozzle radial inflow turbine (VNT), and air-foil bearings [9]. The design and operation of the air management subsystem is described in greater detail in Section 3.

The fuel management subsystem includes a hybrid ejector–hydrogen blower to recirculate the spent anode gas [6]. The ejector operates supersonically with pure hydrogen from the compressed hydrogen tank as the motive gas and the spent hydrogen at the stack outlet as the suction gas. We assume that the motive gas is available at a pressure higher than 15 atm (regarded as the empty tank pressure) and that the suction gas is saturated with water vapor (gas molecular weight of 3–7). The desired lift pressure is 20.7 kPa (3 psi) at rated power and the recirculation ratio (suction gas to motive gas mass flow rate) is 2–5 for 50% hydrogen utilization per pass. Our analysis shows that the ejector alone can recirculate hydrogen for stack power from 100% down to 43% of the rated power [6]. Between 28% and 43% of rated power, a 40-W (mechanical power) blower is needed to assist in recirculating the hydrogen; below 28% of rated power, the motive gas flow and pressure are too low to achieve the required lift pressure and the blower alone recirculates hydrogen. The ejector-only portion of the operating map can be expanded by including a second ejector that is parallel to and smaller than the first ejector; however, the blower is still needed for stack power less than 24%. Alternately, a variable-throat-area ejector can be employed to expand the ejector-only operating window to 36–100% of rated stack power.

The water management subsystem includes a membrane humidifier (MH) for the cathode air and an air pre-cooler. There is no humidifier in the anode circuit, which relies on anode gas recirculation and in-stack water crossover from the cathode air for the humidification of the input hydrogen [6]. The system is designed to be water balanced, i.e., only the water produced in the stack is used for humidifying the feed gases.

The dual-loop heat rejection subsystem has a high-temperature (HT) circuit for supplying coolant to the stack, and a low-

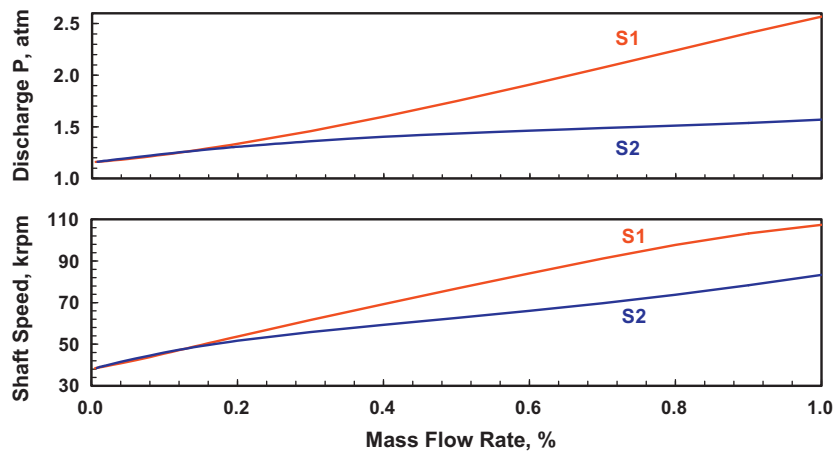


Fig. 2. CEM operating map for 45% FCS efficiency at rated power.

temperature (LT) circuit for supplying coolant to the vehicle traction motor, CEM motor and the air pre-cooler. The coolant in both circuits is aqueous ethylene glycol solution.

We have analyzed the fuel cell system shown schematically in Fig. 1 for values of  $\eta_S(100\%)$  ranging from 35% to 50%, based on the lower heating value (LHV) of hydrogen.

### 3. Air management

We modeled the CEM using component performance maps that were constructed from the experimental data obtained on a full-scale,  $91 \text{ g s}^{-1}$  dry air, unit [9,10]. We applied dimensional analysis methods for centrifugal machines [11] to develop a scalable compressor map from the measured temperature rise for different shaft speeds (rpm) and mass flow rates; the map describes the compressor pressure ratio and efficiency as functions of the corrected shaft speed ( $N_c$ ) and mass flow rate. The expander maps were developed for different nozzle areas from the measured temperature drops for different flow ( $F_f$ ) and velocity ( $F_v$ ) factors; these maps describe the expander pressure ratio as a function of  $F_f$  and  $N_c$  and the expander efficiency as a function of  $F_v$  and the pressure ratio. The efficiency of the 3-phase brushless DC motor was correlated with the motor power and shaft speed. Similarly, the efficiency of the motor controller was correlated with the power to the motor controller and the shaft speed. We also correlated the measured pressure drop across the filter upstream of the compressor with the air flow rate. Finally, the flow rate of the compressed air that is extracted for cooling the motor and the air-foil bearing was measured and correlated with the pressure drop and the shaft speed.

The component maps were incorporated into a model for the compressor, expander and motor that are mounted on a common shaft that is supported on air-foil bearings, with the motor being powered through the motor controller. This model was used to analyze the performance of the CEM in two 80-kW<sub>e</sub> fuel cell systems, in which, at the rated power, one (S1) is pressurized to 2.5 atm (stack inlet pressure) and the other (S2) is pressurized to 1.5 atm. Both systems S1 and S2 use the same configuration as shown in Fig. 1. The model was used to determine the optimum operating points (shaft speed and compressor discharge pressure) at different flow rates (i.e., FCS loads). We found that the CEM component efficiencies are quite comparable for systems S1 and S2. The main difference is that the peak shaft speed for S1 is nearly 110,000 rpm, while the shaft speed is 85,000 rpm for S2 at rated power. The variations in CEM discharge pressure and shaft speed with changing air flows are shown in Fig. 2 for systems with  $\eta_S(100\%)$  of 45%. It may be possible to improve the performance of the CEM in the S2 sys-

tem by redesigning it for a higher speed at 1.5-atm and full flow; the test unit on which the performance data were obtained was designed for 2.5-atm peak pressure.

Based on our model and analyses, the parasitic power consumed by the CEM in the S1 and S2 systems is shown in Fig. 3. For systems with  $\eta_S(100\%)$  of 45%, Fig. 3a presents the CEM power as a function of the net FCS power, where the air mass flow rate varies with changes in the system power level. Fig. 3b shows the CEM power at 100% flow as  $\eta_S(100\%)$  varies over the range of 35–50%. Although the efficiencies of the CEM components are comparable under all S1 and S2 operating conditions, in systems with 45%  $\eta_S(100\%)$ , the CEM consumes  $\sim 10 \text{ kW}_e$  at rated power in S1, but  $< 6 \text{ kW}_e$  in S2. Also, the CEM parasitic power is greater in systems with lower  $\eta_S(100\%)$  that require higher air flow rates (fixed oxygen utilization). The effect of the design-point system efficiency,  $\eta_S(100\%)$ , on CEM parasitic power is somewhat more pronounced in S2 because of the proportionately larger influence of the filter pressure drop on the compression ratio; as  $\eta_S(100\%)$  decreases from 50% to 35%, the CEM motor controller power increases by more than 25% in S2, but only by  $\sim 15\%$  in S1.

Our analyses indicate that the maximum turndown may be limited by compressor surge for CEM shaft speeds less than about 45,000 rpm [6]. At idling conditions, the estimated power consumption is 250–400 W<sub>e</sub>, depending on the allowable minimum shaft speed (Fig. 3a, FCS net power of 8 kW<sub>e</sub> or less). The minimum shaft speed, if lower than the air-foil bearing lift speed of 36,000 rpm, will affect the durability of the air-foil bearings.

Since the automotive fuel cell systems spend little time at the rated power, the overall drive cycle efficiency is more sensitive to the system performance at part load than just at the rated power point [4]. For good part-load efficiency of the FCS, the compressor discharge pressure must be lowered as shown in Fig. 2. The CEM needs an independent means to control the shaft speed and therefore the discharge pressure as a function of the mass flow rate. An actuator, actually a step-up motor, provides the ability to vary the area of the turbine inlet nozzle and thereby control the shaft speed independent of the air flow rate [9]. Our simulations show that near idling conditions, the throat area needs to be throttled down to 15% of the area at full flow rate for both S1 and S2. The simulations also show that the shaft speeds and compressor discharge pressures would be similar in both S1 and S2 at less than 20% of design-point flow rates [6].

### 4. Stack performance

A two-dimensional model [12] was adapted to analyze the performance of a stack with NSTFC based membrane-electrode

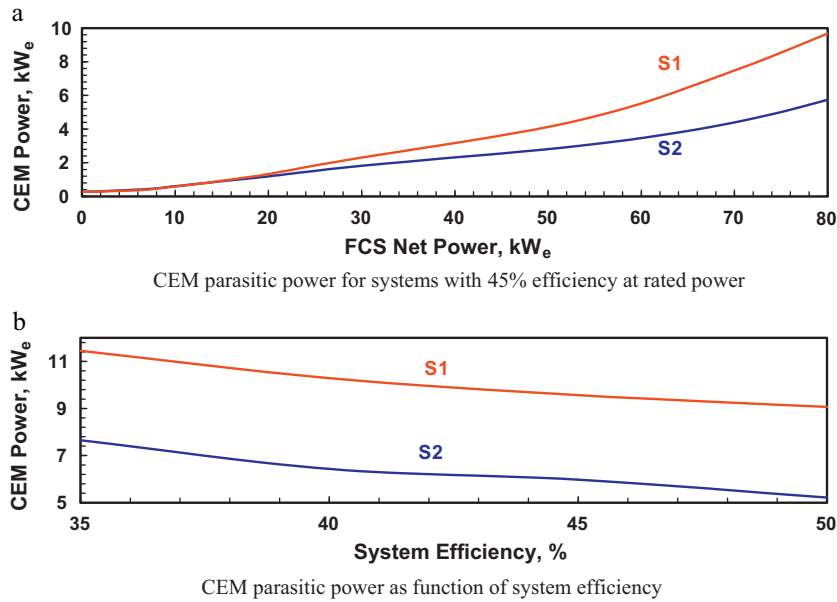


**Fig. 3.** CEM performance for S1 and S2 systems. (a) CEM parasitic power for systems with 45% efficiency at rated power. (b) CEM parasitic power as function of system efficiency.

assemblies. The model solves for the ionic and electric potentials coupled to the transport equations for the charged species, water vapor, liquid water and gaseous species (hydrogen, oxygen and nitrogen) across the five-layer MEA (anode GDL, anode catalyst layer, polymer electrolyte membrane, cathode catalyst layer and cathode GDL) and the anode and cathode flow fields. For brevity, we omit the details and only emphasize the important aspects that are specific to the NSTF catalyst [13], namely the kinetics of the oxygen reduction reaction (ORR), which we represent by a Butler–Volmer type of equation.

$$I + I_x = I_0 L_{Pt} A_{Pt} \left[ \exp \left( \frac{\alpha n F}{RT} \Delta E \right) - \exp \left( - \frac{(1 - \alpha) n F}{RT} \Delta E \right) \right] \quad (1)$$

where  $I$  is the current density,  $\Delta E$  is the overpotential for ORR, and  $F$  and  $R$  are respectively the Faraday and gas constants. The NSTFC specific constants in Eq. (1) were derived from experimental data with 25-cm<sup>2</sup> active area cells [11]. The cyclic voltammetry (CV) data for electrochemical surface area ( $A_{Pt}$ ) were correlated with Pt loading ( $L_{Pt}$ ), relative humidity and temperature ( $T$ ). The measured crossover current density ( $I_x$ ) was used to derive H<sub>2</sub> permeance expressed as a function of the relative humidity and temperature. The exchange current density ( $I_0$ ) and the transfer coefficient ( $\alpha$ ) were determined from the specific activity measurements at 0.9 V for saturated air at 80 °C and 1-atm O<sub>2</sub> partial pressure. The GDL constants for liquid water transport (contact angle) and gas transport (tortuosity) were empirically determined from the mass transfer overpotentials inferred from the polarization curves obtained with a 50-cm<sup>2</sup> active area cell, 150- and 200-kPa inlet pressures, 80 °C cell temperature, 68 °C inlet gas dew points, and 40% O<sub>2</sub> and 50% H<sub>2</sub> utilizations. Also, the high-frequency resistance (HFR) measured by electrochemical impedance spectroscopy (EIS) was used to derive the contact resistance.

We used the stack model to determine the optimum operating conditions for S1 and S2 stacks with a 20- $\mu$ m supported membrane (850 EW), NSTF ternary catalysts with Pt loadings of 0.05 mg cm<sup>-2</sup> on the anode and 0.1 mg cm<sup>-2</sup> on the cathode, and fixed 50% oxygen and hydrogen utilizations. The results of the analyses show that the S1 stack (2.5 atm at rated power) achieves the highest power density at 85 °C, with 64 °C cathode and 59 °C anode inlet dew point temperatures; the corresponding optimum temperatures are lower

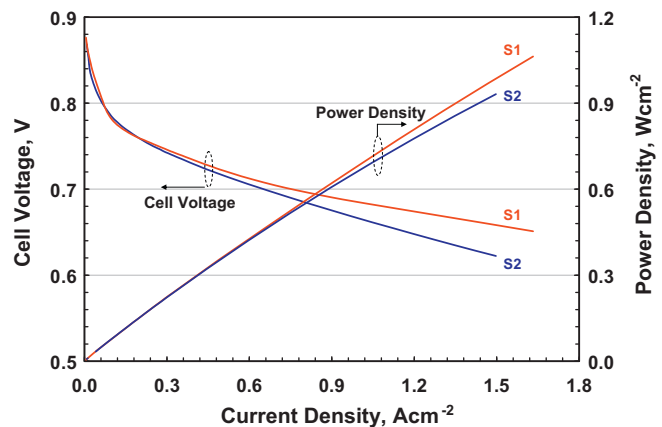


**Fig. 4.** Stack polarization curves for S1 and S2 stacks in systems with 45% FCS efficiency at rated power.

for S2 (1.5 atm at rated power), 75 °C for stack and 61 °C/53 °C cathode/anode inlet dew points. Here, the stack temperature refers to the coolant exit temperature, the anode and cathode streams flow in opposite directions (counterflow), and the coolant flows in the same direction as the cathode air (coflow) with a 10 °C temperature rise across the stack at rated power.

The modeled polarization curves and the stack power density for the S1 and S2 systems are shown in Fig. 4. In these analyses, the operating pressures vary with the current density in accord with the relationship between the optimum pressure and air flow rate shown in Fig. 2. These results show that the cell voltage increases by 20–30 mV at >1 A cm<sup>-2</sup> as the stack operating pressure is raised from 1.5 to 2.5 atm at rated power (with the accompanying increases in operating temperatures and inlet gas relative humidities). In order to realize the benefit of higher operating pressure, the flow field and diffusion media must be carefully designed to maintain limiting currents far in excess of 1 A cm<sup>-2</sup> at the cell operating conditions.

The influence of the design-point system efficiency,  $\eta_s$  (100%), on the cell voltage and power density at the rated power is shown in Fig. 5. The cell voltage in S1 has to be 20–35 mV higher than in S2 to

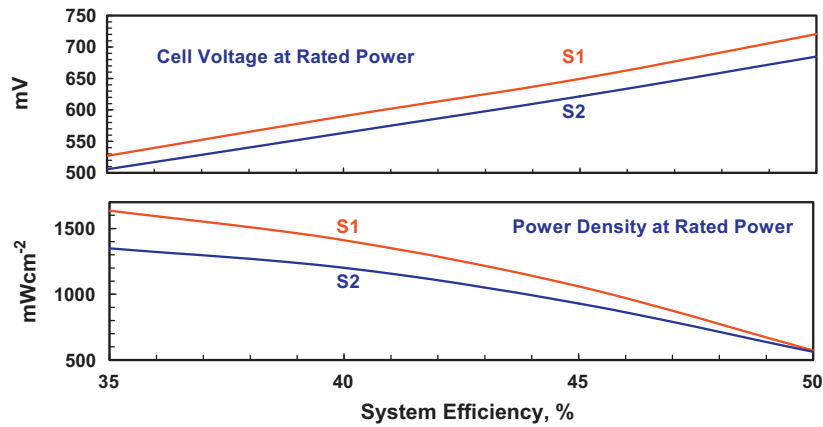


Fig. 5. Stack performance as a function of FCS efficiency at rated power.

compensate for the greater CEM power consumption while achieving the same system efficiency. For either S1 or S2, the cell voltage at rated power is a strong function of  $\eta_S(100\%)$ . For example, in S2, the cell voltage needs to be 685 mV for 50%  $\eta_S(100\%)$ , which decreases to 506 mV if the FCS efficiency is only 35%. Fig. 5 also shows that for the same FCS efficiency, S1 stack has up to 20% higher power density in spite of the higher cell voltage. Moreover, the power density is even a stronger function of the system efficiency (actually cell voltage). It more than doubles (from 573 to 1636  $\text{mW cm}^{-2}$  in S1 and from 561 to 1349  $\text{mW cm}^{-2}$  in S2) if the FCS efficiency at rated power is lowered from 50% to 35%. The flow field and GDL designs are especially important in systems with <40% efficiency, for which the calculated current density is  $>2 \text{ A cm}^{-2}$ , and the thin catalyst layers may flood without proper water management.

Fig. 6 presents the modeled relationship between the Pt content and  $\eta_S(100\%)$ . The results are presented on stack basis (top graph), i.e., g-Pt per  $\text{kW}_e$  gross power produced by stack, and on system basis (bottom graph), i.e., g-Pt per net  $\text{kW}_e$  produced by FCS. Consistent with the power density results shown in Fig. 5, the Pt content in S1 can be up to 20% lower on the stack basis and 15% lower on the system basis than in S2. For either system, the Pt content is a strong function of  $\eta_S(100\%)$ , decreasing by more than 60% (from 0.29 to 0.11 g-Pt  $\text{kW}_{e\text{-net}}^{-1}$  in S1 and from 0.28 to 0.13 g-Pt  $\text{kW}_{e\text{-net}}^{-1}$  in S2) as the required system efficiency at rated power is relaxed from 50% to 35%. Compared to the Pt content required for 50% efficiency at rated power, the Pt content decreases by 45% if the rated power efficiency is lowered to 45%, and by 59% if the  $\eta_S(100\%)$  is lowered to 40%. Further lowering the system efficiency to 35% brings only a 3% marginal saving in Pt content.

## 5. Thermal management

A finite-difference model was developed for heat rejection in cross-flow automotive radiators. We consider a stacked lay-out in which the ambient air heats progressively as it flows across the A/C condenser (9 kW heat load) followed by the low-temperature radiator (LTR, 13–17 kW heat load) and then the high-temperature radiator (HTR). For simplicity, each stacked radiator is assumed to have the same frontal area. The ram air effect on the airside cooling is simulated with assumed pressure recovery/drop coefficients representative of an automotive bumper and grille arrangement for a light-duty passenger vehicle [14]. The airside friction factor ( $f$ ) and the heat transfer coefficients ( $j$ ) were derived from the experimental thermal and fluid mechanics data for 23 cm  $\times$  23 cm  $\times$  3.3 cm sub-scale and 70 cm  $\times$  45 cm  $\times$  3.3 cm full-scale radiators with 18 and 24 fins per inch (fpi) louver fins (LV) and 40 and 50 fpi plain microchannel (MC) fins [15]. We compared the relative perfor-

mance of the four fin geometries tested and concluded that the MC-40 fins are superior to the LV-18 fins in the full-scale design [10]. We also concluded that the FC powertrains may need to be derated at ambient temperatures higher than 40 °C, since the fan power doubles for every 5 °C increase in ambient temperature [6,10].

Fig. 7 shows the effect of FCS design-point efficiency on stack heat load. The results are given for two power levels: full rated power (80  $\text{kW}_e$ ) and partial power (61.5  $\text{kW}_e$ ). Lowering the FCS efficiency at rated power from 50% to 35% decreases the cell voltage at 80- $\text{kW}_e$  from 685 mV to 506 mV (Fig. 7 top) and the corresponding stack efficiency from 53.8% to 39.3% (Fig. 7 middle). The stack heat load, which is proportional to  $P_{\text{PEFC}}(1 - \eta_{\text{PEFC}})/\eta_{\text{PEFC}}$  (where  $P$  is the power and  $\eta$  is the efficiency), increases by 80%, from 72.5 kW to 130 kW (Fig. 7 bottom). Under this condition, the increase in the heat load for the thermal management system may not be manageable, rendering the option of lowering the FCS efficiency at rated power from 50% to 35% as unacceptable.

Consider next the scenario of using an 80- $\text{kW}_e$  stack in a mid-size vehicle (see details in next section) for which the design point for the heat rejection is the thermal load while producing 61.5  $\text{kW}_e$  needed for climbing 6.5% grade at 88  $\text{km h}^{-1}$  (55 mph). In this scenario, the cell voltage corresponding to 61.5  $\text{kW}_e$  is higher, 732 mV vs. 685 mV for the system with 50%  $\eta_S(100\%)$ , and only decreases to 644 mV for the system with 35%  $\eta_S(100\%)$ . Similarly, the stack efficiency is higher (56% vs. 53.8% for the system with 50%  $\eta_S(100\%)$ ) and only degrades to 49% for the system with 35%  $\eta_S(100\%)$ . Also, the stack heat load is lower (49.3 kW vs. 72.5 kW for the system with 50%  $\eta_S(100\%)$ ) and only increases to 63.2 kW for the system with 35%  $\eta_S(100\%)$ . Clearly, the heat rejection task is more manageable in this scenario than in the scenario of rejecting waste heat at full power.

We used the radiator and system models to determine the radiator size required to reject the waste heat produced in the stack. Our analyses showed that on grade the stack temperature must be allowed to rise to 92–95 °C otherwise the required frontal area of the stacked radiators is much larger than 125% of the frontal area in the equivalent ICE vehicles [6]. We also concluded that the PEFC stack pressure has to operate at 2.3–2.4 atm otherwise the membrane dries out [6]. The maximum operating pressure at this condition is primarily limited by the CEM motor power. An expander is needed to reach this elevated pressure even in system S2 in which the expander produces little power at the rated condition [6].

For sustained driving on grade, Fig. 8 shows the total fin area and the fan and coolant pumping power needed to reject the waste heat produced at 61.5  $\text{kW}_e$  and 92–95 °C coolant temperature at

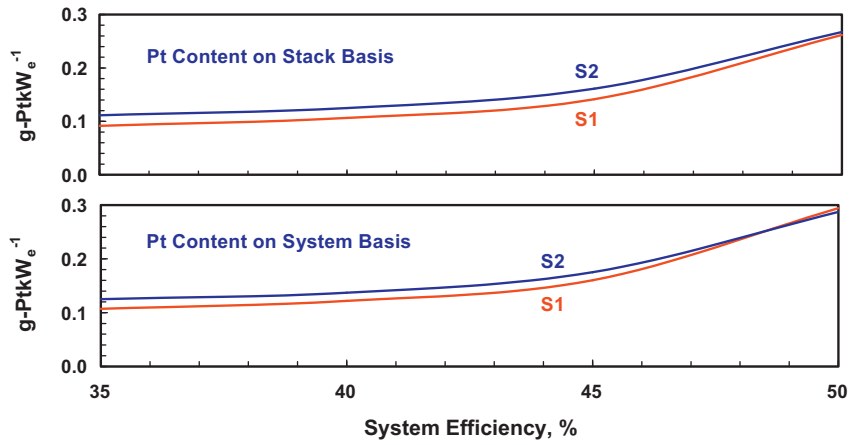


Fig. 6. Stack Pt content as function of FCS efficiency at rated power.

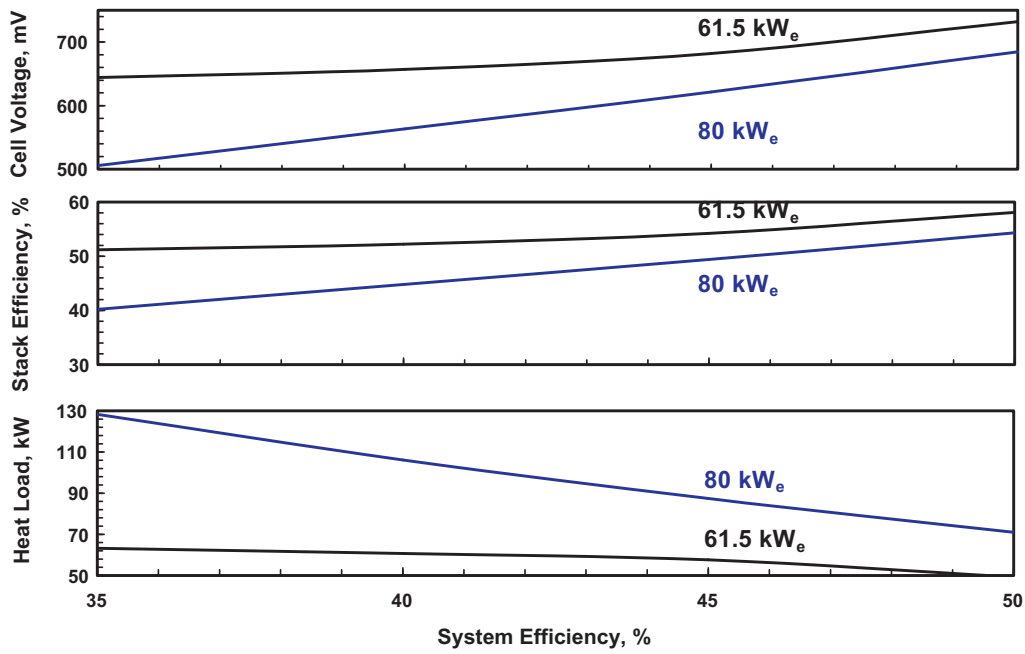


Fig. 7. Heat load on the thermal management subsystem at 100% and 77% power.

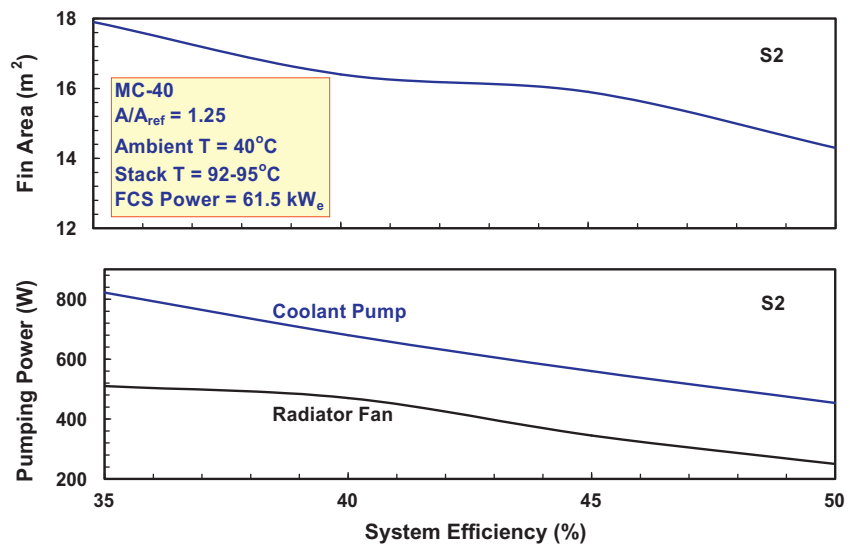


Fig. 8. HTR fin area and coolant and fan pumping power.

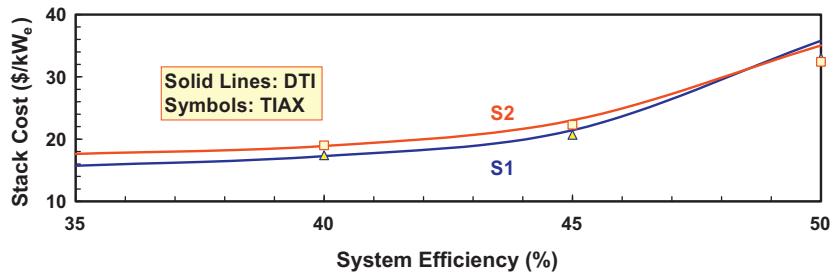


Fig. 9. Estimated cost of PEFC stack at high-volume manufacturing.

stack exit. We find that the HTR fin area is about 20% larger (top graph), the coolant pumping power increases by 60% and the fan pumping power increases by about 90% (bottom graph) if the FC efficiency at rated power is lowered from 50% to 35%. We conclude that heat rejection does become more difficult in the lower efficiency systems, but depending on the vehicle platform, the option of deploying 40–45% efficiency systems should not be excluded from consideration. Also, from the standpoint of heat rejection, the FC systems must be capable of operating at 92–95 °C stack temperatures for short durations (several minutes). It may not be possible to operate the stack at elevated temperatures if the CEM does not include an expander or the FC system does not have a cathode humidifier [6].

6. Stack and system cost

We estimated the costs of the PEFC stacks and systems by using the DTI’s methodology for estimating the costs at high-volume manufacturing (500,000 units per year) [16]. The estimates are based on a design for manufacturing and assembly (DFMA) methodology, but without a markup for the general and administrative (G&A) business expenses, research and development (R&D) expenses, scrap and profit. The costs include direct material costs, manufacturing costs, assembly costs and markup by suppliers of parts and components. The following are the main assumptions used in estimating the costs of the PEFC stack [17].

- The process for manufacturing reinforced membrane rolls consists of two-stage occlusion of the PFSA ionomer on expanded polytetrafluoroethylene web (ePTFE) and drying in an infra-red oven, hydration in boiling water, and drying in air.
- A four-step process is considered for fabricating roll-good NSTF catalyst layers: physical vapor deposition of perylene red on an aluminum-coated film substrate (DuPont Kapton polyamide

web), vacuum annealing to form crystalline nanostructures (organic whiskers) through a screw dislocation mechanisms, vacuum magnetron sputtering of PtCoMn catalyst onto the nanostructures, and transfer of the coated nanostructures to Teflon sheets.

- The manufacturing process flow for the gas diffusion layers assumes that non-woven carbon substrate (macroporous layer) is procured as rolls to which a hydrophobic microporous layer of PTFE and Vulcan XC-72 is applied.
- The process flow for the metal bipolar plates consists of progressive stamping of Fe–20Cr–4V sheets to form the flow field and thermally grown chromium nitriding for corrosion protection.
- A three-step process is considered for assembling the MEA: (1) hot-pressing of the catalyzed membrane with the two GDLs, (2) cutting and slitting of the hot-pressed membrane and electrodes into rectangular pieces, and (3) inserting the pieces into a mold with the frame/gasket around it.
- The end plates are a compression-molded composite (LYTEX 9063), strong enough to withstand the required compressive loading while also being sufficiently electrically non-conductive. Two copper current studs protrude through the end plates to connect to a copper sheet (which may need to be coated to prevent corrosion in air) in contact with the last bipolar plates.
- After considering different methods of manufacturing and applying gaskets, a laser-welding process was selected for the metallic coolant gaskets and a screen-printing method was selected for the end gaskets.
- Instead of the traditional tie rods, metallic compression bands are assumed to be used for stack compression.
- At high production rates, stack assembly is semi-automatic, i.e., the end-components are assembled manually but the repeat units are assembled via an automated fixture. Following assembly, each stack is transported to a leak-check station to verify gas and liquid sealing. A voltage variation method was selected for stack conditioning. Conditioning cost is calculated by estimating the capital cost of a programmable load bank to run the stacks up and down the polarization curve according to the power-conditioning

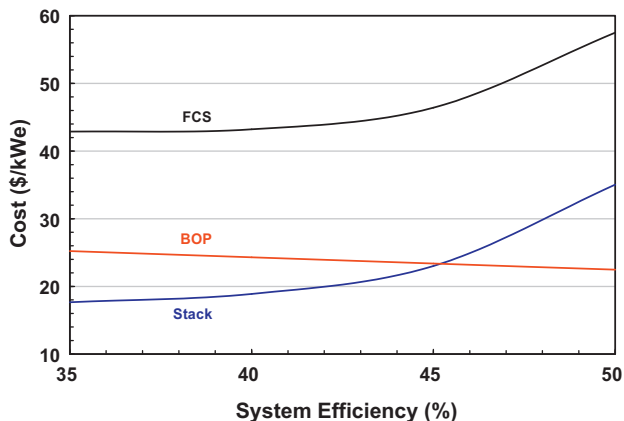


Fig. 10. Estimated cost of FC system at high-volume manufacturing.

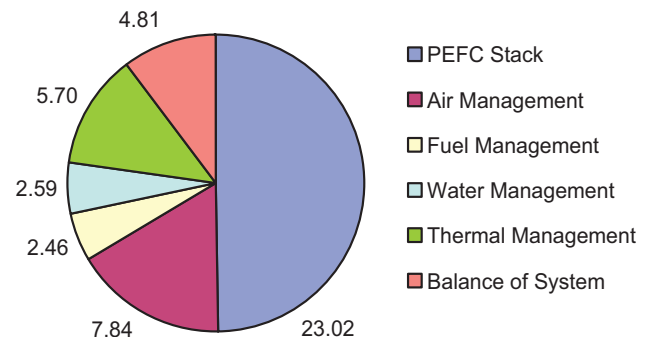


Fig. 11. Cost breakdown for S2 system with 45% efficiency at rated power.

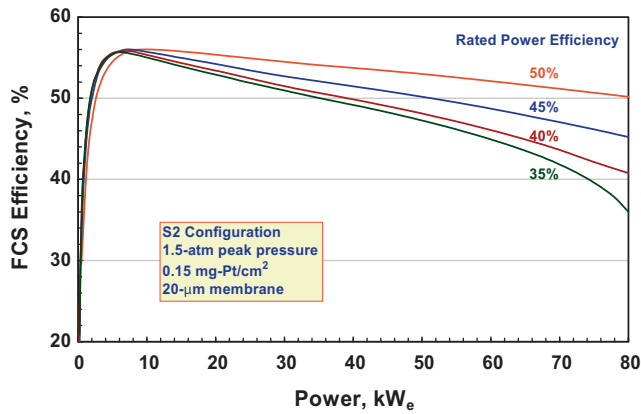


Fig. 12. Part-load performance of S2 systems with different efficiency at rated power.

regimen. The conditioning process also serves as a stack quality control, and no further system checkout is included in the manufacturing process.

The stack cost model was run parametrically and multi-variable regression was performed to correlate stack cost (\$ per  $\text{kW}_e$  gross power) with active membrane area, catalyst loading, Pt price and stack voltage [17]. The range of validity for the cost correlation is 60–120  $\text{kW}_e$  gross stack power, 0.1–0.8  $\text{mg cm}^{-2}$  total Pt loading (anode plus cathode), 7–16.5  $\text{m}^2$  total active membrane area, \$800–2000 per troy-ounce Pt price, and 150–300 V stack voltage. We used the correlation to estimate the high-volume manufacturing cost of the stack as a function of the FCS efficiency at rated power, and the results are presented in Fig. 9 for assumed \$1100  $\text{troz}^{-1}$  (\$35  $\text{g}^{-1}$ ) price for Pt. Also included, as triangle symbols for system S1 and square symbols for S2, are the comparable results from a different cost model with identical inputs, but with slightly different manufacturing assumptions [18]. The results show that the S1 stack operating at 2.5 atm can be 12% less expensive than the S2 stack for 35% FCS efficiency at rated power; the differences in S1 and S2 stack costs are less pronounced at higher system efficiencies. We calculate that decreasing the S2 rated-power efficiency from 50% to 35% results in a 56% reduction in Pt requirement and a 50% reduction in the projected stack cost (from \$35.0 to \$17.7  $\text{kW}_e^{-1}$ ). Compared to the 50%-efficiency S1 system, the projected saving in stack cost is 34% for a 45%-efficient system and 46% for a 40%-efficient system.

Table 1  
FC HEV component specifications.

Configuration	Series FC HEV
Transmission	2 speed manual = 1.86, 1 Peak efficiency = 97.5%
Final drive	Ratio = 4.44, constant efficiency = 97.5%
Wheels	Wheel radius = 0.317 m Rolling resistance = 0.0075 ( $C_0$ ), 0.00012 ( $C_1$ )
Vehicle	Gross vehicle weight = 1595 kg $C_D = 0.26$ , $A_F = 2.2 \text{ m}^2$ Ballard IPT 300 V, peak efficiency = 95%
Traction motor	Peak power = 97.8 kW
ESS	Li-ion, no. of cells = 62, peak power = 40 kW
FCS	Rated power = 80 kW Rated power efficiency = 35–50%
DC–DC converter	Constant efficiency = 95%

We have also developed and used correlations for estimating the cost of the balance-of-plant (BOP) components in the fuel cell system. As discussed below, however, the BOP cost estimates are based on a less rigorous methodology than the DFMA-style analysis methodology used for the stack.

- The cost of the air management subsystem (compressor, expander, air-foil bearing, motor, motor-controller, air filter and housing, stack manifolds for air inlet and air outlet, and an air mass flow sensor) is based on a bottom-up cost analysis. A regression analysis was performed to correlate the cost of the air management subsystem with compressor discharge pressure (1.5–2.5 atm) and air flow rate (80–180  $\text{g s}^{-1}$ ).
- The cost of the water management system is based on a DFMA-style analysis of the membrane humidifier, experience-based analysis of the air precooler and market analysis of the demister. Regression analyses were used to correlate the humidifier cost with the membrane area (2–6  $\text{m}^2$ ) and the precooler cost with the heat load (1–10 kW) and the temperature difference (40–80 °C) driving force for heat transfer.
- The cost of the thermal management subsystem is based on the available information for standard automotive components (radiator fans, coolant pumps, radiators, coolant DI filter, thermostatic valve). The regression analysis correlated the cost of the thermal subsystem (high temperature and low-temperature cooling loops) with the heat duty, temperature difference, and radiator fan power.
- The cost of the fuel management subsystem (hydrogen recirculation blower, ejector, pressure regulator, purge valve and check valve) is based on experience and postulated scaling laws. The

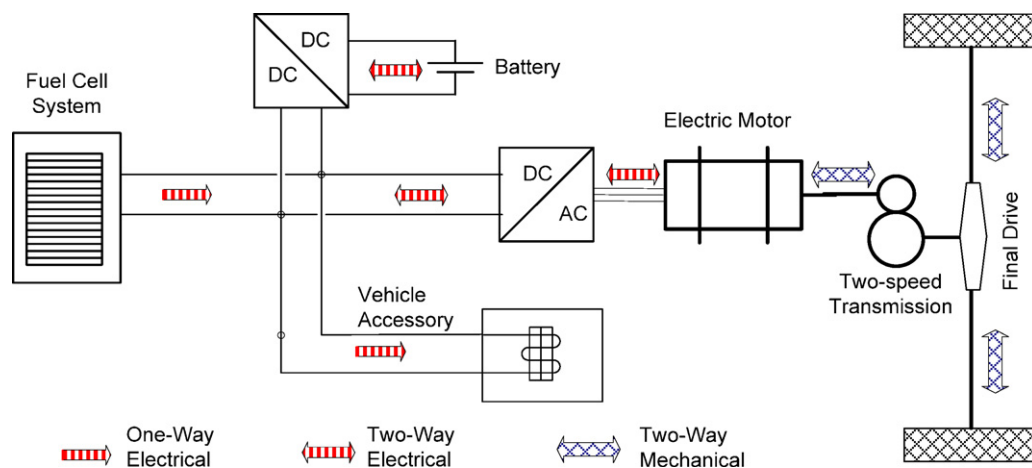


Fig. 13. Configuration of the modeled FC series hybrid electric vehicle.

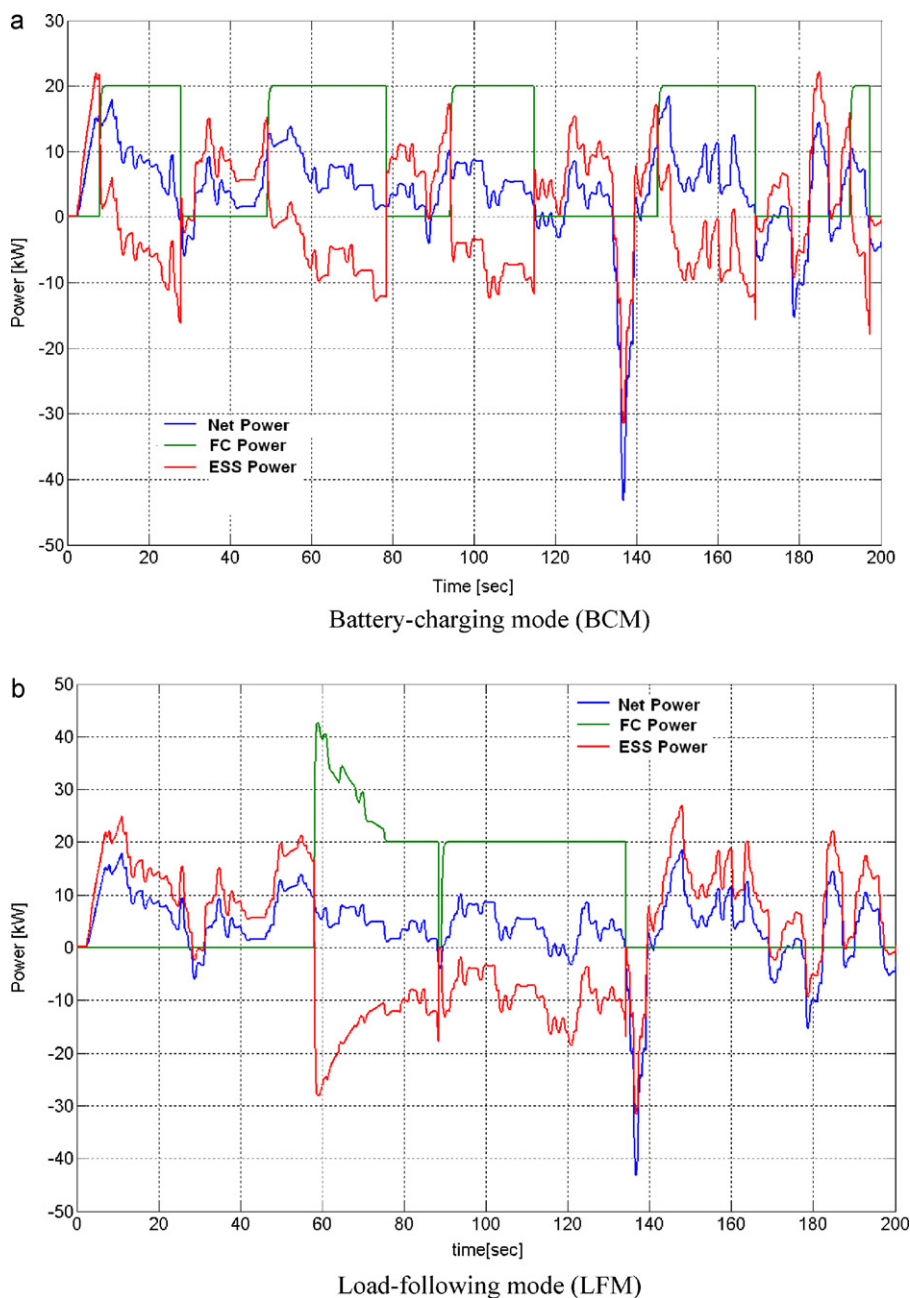


Fig. 14. Illustration of the energy management strategies for battery-charging and load-following modes. (a) Battery-charging mode (BCM). (b) Load-following mode (LFM).

regression analysis correlated the combined cost of the subsystem with the blower power (50–1500 W).

- The cost of the balance of the system (system controllers, hydrogen sensors, belly pan, wiring, ducting, tubing and piping for hydrogen, air and coolant, and system assembly and testing) was treated as constant across the fuel cell power ratings considered.

Fig. 10 presents the cost of the BOP and FCS at high-volume manufacturing. Whereas the stack cost decreases at lower system efficiencies, the cost of the BOP increases as the system design-point efficiency is reduced. At lower efficiencies, the costs of the air and water management subsystems increase because of higher air flow rates, the fuel management subsystem becomes costlier because of higher volumetric flow rate of the recirculating fuel stream, and the cost of the thermal management subsystem increases because of higher heat rejection rates. Compared to the overall cost of the

50%-efficient FCS ( $\$57.51 \text{ kW}_e^{-1}$ ), we project a 19% decrease in the overall cost if we accept a 5%-point lower efficiency ( $\$46.41 \text{ kW}_e^{-1}$  for 45% efficiency). The overall cost can decrease by a further 6% if we accept a 10%-point reduction in design-point system efficiency ( $\$43.22 \text{ kW}_e^{-1}$  for 40% efficiency). The incremental saving in the overall system cost is about 1% point for FCS efficiencies less than 40%.

Fig. 11 provides a breakdown of the cost ( $\$ \text{ kW}_{e-\text{net}}^{-1}$ ) of the individual subsystems for the FC system with 45%  $\eta_s$  (100%). The PEFC stack accounts for nearly 50% of the overall cost. The air management subsystem is the next most expensive component, accounting for 17% of the overall cost, followed by the thermal management subsystem, which accounts for 12% of the overall cost. The fuel management and water management subsystems contribute almost equally to the overall cost (11% combined). Clearly, substantial simplification in BOP components and functionality is

needed to achieve the long-term cost target of  $\$10 \text{ kW}_e^{-1}$ , and the simplification will have to occur in all of the ex-stack subsystems.

## 7. System performance at part load

We have analyzed the part-load performance of the S2 system. The air stoichiometry was held constant, subject to the constraint of the maximum turndown of the CEM. The stack temperature and inlet operating pressures were determined for maximum efficiency. With a fixed humidifier, the stack inlet humidity is a function of many variables including the air flow rate, temperature of the spent air (same as the stack temperature) and operating pressure [4,6]. At part load, reduced throughput in the humidifier tends to increase the water mass transfer rate (the stack inlet RH) but the lower pressure has the opposite effect. Similarly, the stack performance generally improves with increasing pressure (higher Nernst potential, lower activation overpotential), but it is also affected by the inlet RH (possibility of flooding). The parasitic power consumed by the CEM also increases with increasing compressor discharge pressures. We captured these interdependencies by simulating the joint performance of the CEM, membrane humidifier, and the PEFC stack with flow connections as shown in Fig. 1. We employed an optimization algorithm to determine the best operating points, and conducted additional parametric searches in the operating space where the algorithm failed to converge [4,6].

Fig. 12 presents the calculated optimum steady-state efficiencies at part load for an S2 system with design-point efficiencies ranging from 35% to 50%. The system efficiency increases as the load is reduced from 100% to 10% of rated power, primarily because of the improvement in stack efficiency as the cell voltage increases with decreasing power generation in the stack (see Fig. 4). The increase in system efficiency is less than the increase in the stack efficiency, however, because of many factors that combine to reduce the FCS efficiency at very low loads. The efficiency loss because of hydrogen crossover (varies inversely with pressure but also depends on RH) becomes important at low loads. Similarly, nitrogen crossover from cathode to anode becomes important at low loads since increasingly larger amounts of hydrogen have to be purged from the anode recycle stream to limit the buildup of nitrogen [17]. The efficiencies of the CEM components decrease at low loads, and the air flow rate cannot be decreased further once the maximum CEM turndown limit is reached. The net result of these loss mechanisms is that the system efficiency peaks at about 10% of the rated power, even though the voltage efficiency (ratio of cell voltage to Nernst voltage) continues to increase as the power draw from the FCS decreases to below 10% of the rated power.

Fig. 12 also shows that the peak efficiency is quite insensitive to the FCS efficiency the rated power, changing by less than 1% as the rated-power efficiency is lowered from 50% to 35%. Furthermore, there can be an inverse relationship between the rated-power efficiency and the system efficiency for power less than 10% since the systems with higher  $\eta_S(100\%)$  have lower power density, larger membrane area and, therefore, greater hydrogen and nitrogen crossover.

## 8. Drive-cycle performance

We have conducted simulations of a battery-FCS hybrid electric vehicle (HEV) to determine the relationship between the rated power efficiency and the system efficiency over selected drive cycles. A mid-size family sedan was selected as the reference vehicle platform, for which Table 1 lists the major parameters that affect its fuel economy. These parameters include the vehicle mass, drag coefficient ( $C_D$ ), frontal area ( $A_F$ ), and the coefficients of rolling friction ( $C_0$  and  $C_1$ ).

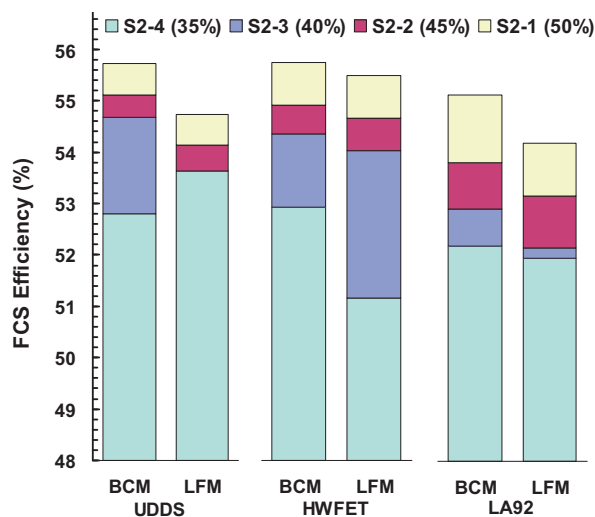


Fig. 15. Drive cycle efficiency as function of FCS efficiency at rated power.

Fig. 13 shows the configuration of the vehicle power train considered in this study [18,19]. The DC input voltage to the inverter for the AC traction motor floats with the output voltage of the PEFC stack as the two are coupled directly. A bi-directional DC/DC converter is used to step-up the voltage of the battery pack to match the PEFC stack voltage during discharge or to step-down the inverter/rectifier output voltage to the appropriate level for charging the battery during regenerative braking. The DC/DC converter is assumed to have an average efficiency of 95% in both the step-up and step-down modes. The mechanical energy at the motor shaft is transmitted to the wheels via a two-speed transmission (gear ratios selected for 100-mph top speed and 0–60 mph acceleration in 60 s) and a final drive (differential with specified gear ratio). The operating map of the three-phase AC induction electric motor (efficiency as function of torque and speed) with 97.8 kW peak power and 95% peak efficiency was constructed from tests with a sub-scale unit [20,21]. In our simulations, we used a Li-ion battery pack, tested in our laboratory, as the energy storage system (ESS), each cell of which has a rated  $C_5$  capacity of 6 A-h with 2.9–4.0 V safe (continuous) operating voltage range.

The simulations were run for two charge-sustaining modes of operation, one in which the FCS is operated primarily as a battery charger (BCM), and the second in which it is operated in the load-following mode (LFM). These two modes of operation are shown in Fig. 14, which shows the vehicle power demand at the wheels ( $P_V$ , blue curves), power supplied or absorbed by the ESS (red curves) and power supplied by the FCS (green curves) over a 200-s span of a drive cycle (For interpretation of the references to color in text, the reader is referred to the web version of the article.). The energy management is done through the ESS in the battery charging mode, i.e., the ESS power follows the vehicle load and the FCS is turned on when the ESS state of charge (SOC) drops below the minimum limit ( $\text{SOC}_{\min} = 0.5$ ) or if the ESS cannot match  $P_V$ . If the FCS is on, it is operated at the peak efficiency point ( $P_{\text{FCS}}(\eta_{\max})$ ) if  $P_V$  is less than  $P_{\text{FCS}}(\eta_{\max})$ . The FCS is turned off when the SOC exceeds the maximum limit ( $\text{SOC}_{\max} = 0.7$ ). The ESS is auxiliary to FCS in LFM, i.e., the FCS power follows the vehicle load. If SOC is less than  $\text{SOC}_{\max}$ , the FCS is operated at  $P_{\text{FCS}}(\eta_{\max})$  during the time that  $P_V$  is less than  $P_{\text{FCS}}(\eta_{\max})$ . In the current simulations, the FCS does not idle; instead, it is turned off when the total power demand (sum of  $P_V$  and ESS charging power) is less than  $4 \text{ kW}_e$ . As in BCM, the ESS power follows the load during the time that the FCS is turned off, and the FCS is turned on if the SOC drops below  $\text{SOC}_{\min}$  or the ESS cannot match  $P_V$ .

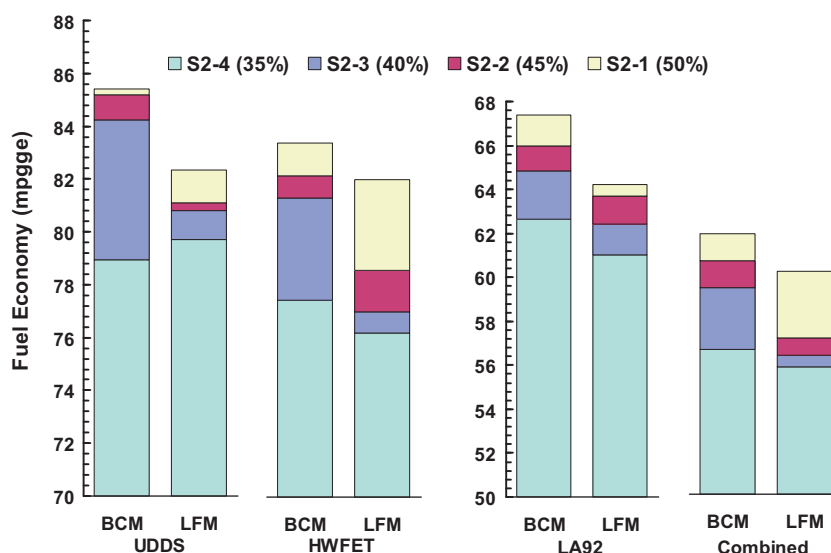


Fig. 16. Unadjusted and adjusted fuel economy on drive cycles.

We ran simulations over three drive cycles [20,21]: mild highway drive cycle (HWFET), more aggressive stop-and-go urban drive cycle schedule (UDDS), and an even more aggressive Los Angeles drive cycle (LA92). Fig. 15 presents the net FCS efficiency, defined as the total kWh<sub>e</sub> produced by the FCS divided by the LHV of the fuel consumed over these drive cycles. As expected, the net FCS efficiencies are higher in BCM than in LFM, but the FCS durability may be an issue because of the excessive number of starts and stops. On UDDS, the two energy management strategies involve 58 FCS start-stops in BCM and only 4 in LFM. These FCS start-stops can be eliminated altogether if the fuel cell is allowed to idle at low loads rather than being turned off. On the three cycles analyzed, the FCS net efficiency can be up to 1.8% higher in BCM than in LFM, and the net efficiencies are lowest on LA92, the most aggressive cycle.

Our simulations indicate that the drive-cycle FCS efficiency is equally sensitive to the rated-power FCS efficiency in LFM and BCM even though the FCS spends more time near the peak efficiency in BCM and the peak efficiency only weakly depends on rated power efficiency. The net efficiency in LFM is most sensitive to the rated power efficiency on HWFET than UDDS, primarily because the ESS power management algorithm used in our model is not optimized for any one particular cycle. The LFM simulations indicate that reducing the rated-power efficiency from 50% (S2-1) to 35% (S2-4) results in 1.0% difference in net FCS efficiencies on UDDS, 4.3% on HWFET, and 2.3% on LA92.

Fig. 16 presents unadjusted fuel economy on UDDS, HWFET and LA92 drive cycles and the adjusted fuel economy on the combined cycle used by EPA for window certification [20,21]. Our simulations indicate that the fuel economy can be up to 4.3% higher in BCM than in LFM. The fuel economy differences between the two modes are more pronounced on the more aggressive cycles (LA92 > UDDS > HWFET). The fuel economies in BCM and LFM are actually higher on the more aggressive UDDS than HWFET because of regenerative braking and the fixed energy management protocol used in our simulations that favors UDDS. Our LFM simulations indicate that reducing the rated-power efficiency from 50% to 40% results in 1.9% lower fuel economy on UDDS, 6.5% on HWFET, 2.8% on LA92, and 6.7% on the combined cycle.

## 9. Summary and conclusions

We have conducted a trade-off study to understand the influence of lowering the rated power efficiency of a fuel cell system

on its part-load performance, drive cycle performance, stack and system costs, and heat rejection. The reference PEFC stack chosen for the study uses mechanically supported, thin (20- $\mu\text{m}$ ), modified PFSA membranes; nanostructured, thin-film ternary catalysts with ultra-low Pt loading (0.15 mg-Pt cm<sup>-2</sup>); and organic whiskers as catalyst supports.

The results from our study indicate that lowering the rated power FCS efficiency from 50% to 40% decreases the Pt content by 50%, from 0.29 to 0.14 g-Pt kW<sub>e</sub><sup>-1</sup>, the projected stack cost at high-volume manufacturing by >46%, from \$33 to \$18.9 kW<sub>e</sub><sup>-1</sup>, and the projected system cost at high-volume manufacturing by 25%, from \$57.5 to \$43.2 kW<sub>e</sub><sup>-1</sup>. The stack heat load, however, increases by 50% at full power (80 kW<sub>e</sub>) and by 23% at the continuous power (61.5 kW<sub>e</sub>) needed to propel the modeled mid-size passenger car on 6.5% grade at 55 mph. The corresponding penalties in the performance of the modeled FC HEV are: a <1% reduction in the FCS peak efficiency; decreases in the drive-cycle efficiencies of 2% on UDDS, 2.7% on HWFET, and ~4% on LA92 drive cycles; and a 6.3% decrease in the fuel economy on the combined cycle used by EPA for fuel economy and emission certification.

The advantages of further lowering the rated power efficiency from 40% to 35% are relatively small: a 5.2% reduction in the Pt content, a 3.5% decrease in the PEFC stack cost, and a 2% decrease in the FC system cost. The corresponding penalties are a 31% increase in the stack heat load at full power (5% at 61.5 kW<sub>e</sub>), a 2–4% decrease in the drive-cycle efficiency on UDDS, HWFET and LA92 cycles, and a 1% decrease in the fuel economy on the combined EPA cycles.

Our study indicates that heat rejection becomes more challenging as the FCS efficiency at rated power is lowered from 50% to 40%. The challenge is less stringent if the FCS is used in a vehicle platform for which the design point for the heat rejection system occurs at partial load. Moreover, the FC system must allow the stack temperature to rise to 90–95 °C under driving conditions where heat rejection is difficult. It may not be possible to raise the stack temperature without raising the stack pressure, otherwise the membrane dries out and the heat load increases in the process. Thus, the air management system must have the capability to operate at higher than normal pressures under difficult thermal management conditions.

## Acknowledgements

This work was supported by the Fuel Cell Technologies Program of the U.S. Department of Energy's Office of Energy Efficiency and Renewable Energy.

## References

- [1] R.K. Ahluwalia, X. Wang, J. Power Sources 177 (2008) 167–176.
- [2] M.K. Debe, J.M. Larson, W.V. Balsimo, A.J. Steinbach, R.J. Ziegler, Membrane electrode assemblies, United States Patent, US 6,613,106, September 2003.
- [3] A. Bonakdarpour, K. Stevens, G.D. Vernstrom, R. Atanasoski, A.K. Schmoeckel, M.K. Debe, J.R. Dahn, Electrochim. Acta 53 (2007) 688–694.
- [4] R.K. Ahluwalia, X. Wang, J. Power Sources 139 (2005) 152–164.
- [5] J. Sinha, Y. Yong, S. Lasher, P. Kopf, Manufacturing cost analysis of direct-hydrogen PEM fuel cell systems for automotive applications: 2008 updates, TIAX Report D0362, November 2009.
- [6] R.K. Ahluwalia, X. Wang, K. Tajiri, R. Kumar, Fuel cell systems with low platinum loadings, DOE Hydrogen Program, FY 2010 Annual Progress Report, 2010.
- [7] M.K. Debe, A.K. Schmoeckel, G.D. Vernstrom, R. Atanasoski, J. Power Sources 161 (2006) 1002–1011.
- [8] M.P. Brady, H. Wang, J.A. Turner, H.M. Meyer, K.L. More, P.F. Tortorelli, B.D. McCarthy, J. Power Sources 195 (2010) 5610–5618.
- [9] M.K. Gee, Cost and performance enhancements for a PEM fuel cell system turbocompressor, FY 2005 Annual Progress Report, DOE Hydrogen Program, 2005, pp. 985–988.
- [10] R.K. Ahluwalia, X. Wang, R. Kumar, Fuel cell systems analysis, DOE Hydrogen Program, FY 2007 Annual Progress Report: V.A.1 Fuel Cells/Analysis/Characterization, November 2008, pp. 793–797.
- [11] P.G. Hill, C.R. Peterson, Mechanics and Thermodynamics of Propulsion, Addison-Wesley Publishing Co., Reading, MA, 1970, November.
- [12] R.K. Ahluwalia, X. Wang, J. Power Sources 162 (2006) 502–512.
- [13] M.K. Debe, Advanced Cathode Catalysts and Supports for PEM Fuel Cells, DOE Hydrogen Program, Washington, DC, 2010.
- [14] U.W. Schaub, H.N. Charles, Ram air effects on the air side cooling system performance of a typical North American passenger car, SAE 800032, 1981, pp. 172–188.
- [15] Z. Mirza, Development of Thermal and Water Management System for PEM Fuel Cell, DOE Hydrogen Program, Washington, DC, 2010.
- [16] B. James, J. Kalinoski, K. Baum, Mass-production Cost Estimation for Automotive Fuel Cell Systems, DOE Hydrogen Program, Washington, DC, 2010.
- [17] B.D. James, J.A. Kalinoski, K.N. Baum, Mass Production Cost Estimation for Direct H<sub>2</sub> PEM Fuel Cell Systems for Automotive Applications: 2009 Update, DTI Report GS-10F-0099J, January 2010.
- [18] J. Sinha, Direct Hydrogen PEMC Manufacturing Cost Estimation for Automotive Applications, DOE Hydrogen Program, Washington, DC, 2010.
- [19] R.K. Ahluwalia, X. Wang, J. Power Sources 171 (2007) 63–71.
- [20] R.K. Ahluwalia, X. Wang, A. Rousseau, R. Kumar, J. Power Sources 130 (2003) 192–201.
- [21] R.K. Ahluwalia, X. Wang, J. Power Sources 152 (2005) 233–244.